

# Self-Organization of Nanoscale Multilayer Liquid Metal Films: Experiment and Theory

Hare Krishna,<sup>†</sup> Nozomi Shirato,<sup>‡</sup> Sagar Yadavali,<sup>§</sup> Ritesh Sachan,<sup>‡,⊥</sup> Jeremy Strader,<sup>§,⊥</sup> and Ramki Kalyanaraman<sup>‡,§,⊥,\*</sup>

<sup>†</sup>Department of Physics, Washington University, St. Louis, Missouri 63130 and <sup>‡</sup>Department of Materials Science and Engineering, <sup>§</sup>Department of Chemical and Biomolecular Engineering, and <sup>⊥</sup>Sustainable Energy Education and Research Center, University of Tennessee, Knoxville, Tennessee 37996

**ABSTRACT** Surfaces made from composite nanostructured materials are potential multifunctional platforms for detection, sensing, and energy harvesting in biological and inorganic systems. However, robust and cost-effective synthesis routes are required to create the required arrays of nanostructures with tailorable size, morphology, and composition. Here we show that self-organization *via* spontaneous pattern formation in nanometer thick bilayer liquid films could lead to such nanostructure arrays. Experimentally, bilayers of immiscible metallic liquids show different self-organized patterning characteristics based on their order of arrangement on a substrate. Energy rate theory based on equating the rate of free energy change to viscous dissipation was used to explain this result. The different bilayer arrangements change the signs of intermolecular interactions, which changes the mode of coupled deformations and the patterning characteristics. Patterning length scale characteristics from nanosecond pulsed laser induced self-organization of Ag and Co liquids on SiO<sub>2</sub> substrate were in good agreement with theory.

**KEYWORDS:** self-assembly · metal · liquid · bilayer · thin film · nanostructure · laser · dewetting · plasmon · silver · cobalt

**F**uture multifunctional materials that combine various physical effects, such as ferromagnetism, strong localized surface plasmon resonance, magneto-optics, and catalysis, could be made from mixtures and/or alloys of multiple metals. Surfaces composed of such nanomaterials will enable unique platforms to perform biocatalysis and biosensing<sup>1–3</sup> as well as to control the polarization and current of photons and electrons.<sup>4–6</sup> Since the resulting properties of such nanomaterials will be determined by size, spacing, shape, and composition, appropriate cost-effective synthesis techniques must be investigated. Toward this goal, nanoscale pattern forming techniques, for example, by energetic beam irradiation, could be very useful.<sup>7–11</sup> Alternately, a self-organizing route, in which intrinsic material parameters control nanostructure formation, is a strong candidate because of the inherent predictability and robustness of such a process. One example of such a process is the classical spinodal

dewetting of ultrathin films in which intermolecular forces determine the length scales of pattern formation. Pattern formation and the ensuing nanostructure is a result of an instability arising when the stabilizing surface tension force is overcome by destabilizing attractive intermolecular dispersion forces.<sup>12,13</sup> Since surface tension and intermolecular forces are intrinsic, depending primarily on the materials making up the film and substrate, the resulting spinodal dewetting length scales are very predictable.

In this work, we present the first experiments and use of energy rate (ER) theory to explore spontaneous self-organization (SO) in bilayer metallic liquid films that result in nanostructured arrays with predictable length scales. It has been shown previously that spinodal dewetting in single layer films with high melting points, such as the metallic films, can be initiated and progressed by multiple cycles of melting by a nanosecond pulsed laser.<sup>14,15</sup> Here, we have applied the technique to bilayers of Ag/Co (AGCO) and Co/Ag (COAG) on SiO<sub>2</sub> surfaces. Co and Ag were selected because they are immiscible and are promising for ferromagnetic-plasmonic applications.<sup>16</sup> The morphologies of the resulting SO patterns were similar in nature to that of spinodal dewetting in single layer metal films (Figure 1).<sup>15</sup> However, investigations of the SO length scales revealed dramatic differences in behavior for the two bilayer arrangements. The AGCO showed a non-monotonic behavior, that is, an increase followed by a decrease and eventual saturation with increasing top Ag thickness (Figure 2a). However, COAG showed a monotonic increase in length scale with increasing top Co layer thickness (Figure 2b).

\*Address correspondence to ramki@utk.edu.

Received for review September 2, 2010 and accepted December 10, 2010.

Published online December 22, 2010.  
10.1021/nn1022632

© 2011 American Chemical Society

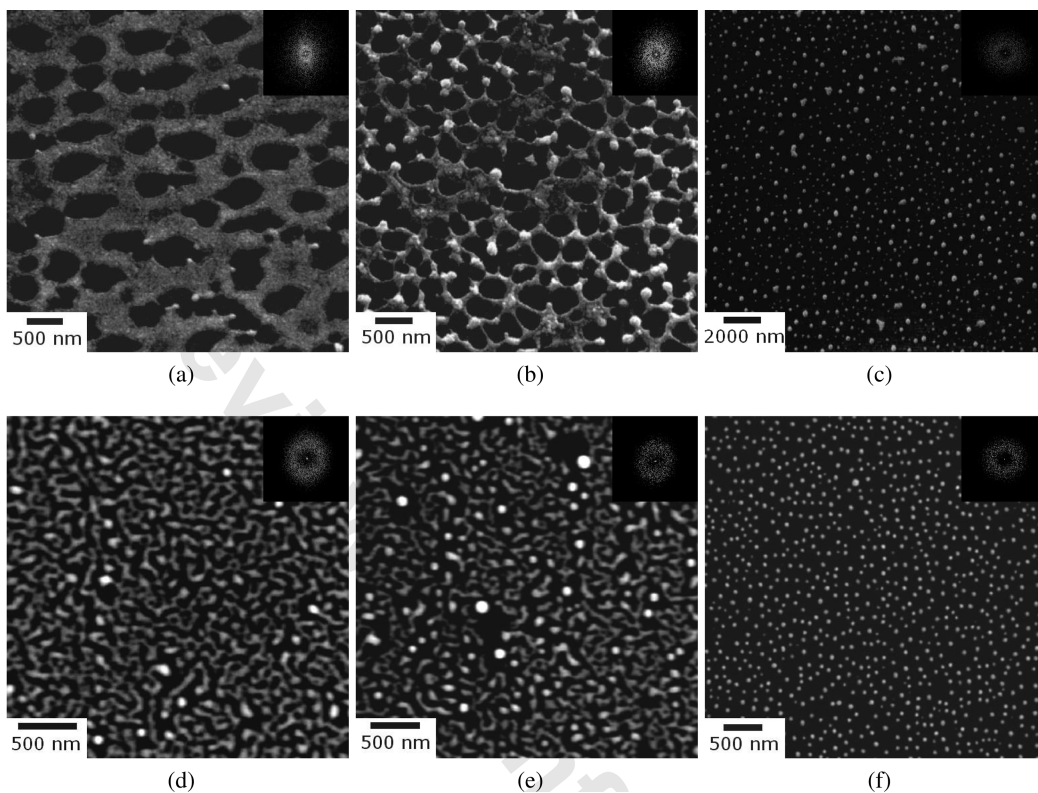


**Figure 1.** SEM images for the morphological evolution in the two bilayer configurations. (a–c) Morphology after irradiation on the Ag/Co/SiO<sub>2</sub> bilayer with 1 nm of Ag and 5 nm Co. (d–f) Morphology after irradiation on the Co/Ag/SiO<sub>2</sub> bilayer with 1.5 nm of Co and 5 nm Ag thickness. The images (a,d), (b,e), and (c,f) are after irradiation with 10, 100, and 10 000 laser pulses. The inset of each image shows the FFT of the corresponding SEM image. The annular shape in each FFT is an indication of the presence of SRO.

In order to explain this difference in SO behavior, we have applied the ER model based on fluid flow equations for bilayer systems developed previously by Ban-dopadhyay and co-workers<sup>17</sup> and Pototsky and co-workers.<sup>18</sup> In this thermodynamic or ER model, the dispersion relation characterizing the growth rate of wave vectors during SO is obtained by equating the rate of Gibbs free energy change ( $\Delta F$ ) with viscous dissipation ( $E_V$ ) in the bilayer fluid flow.<sup>19</sup> We recently applied this model to single layer films and found the utility of this linear theory to be in its rapid prediction of SO length scales, similar to linear stability analysis, as well as in providing additional physical insight into the nature of fluid flow.<sup>20,21</sup> The results presented here show that ER accurately captures the experimental behavior for the two bilayer arrangements. The fundamental reason for the different SO behavior is the difference in sign of intermolecular forces for the two arrangements. As a result, theory shows that AGCO deforms by the bending mode, that is, when perturbation of the top surface and intermediate liquid/liquid interface are in phase with each other. On the other hand, COAG deforms by the squeezing mode, in which the two perturbations are completely out of phase with each other.

## RESULTS

**Experiment.** Figure 1a–c shows a series of SEM micrographs of the evolution of the morphology in bilayer

Ag/Co/SiO<sub>2</sub> as a function of number of laser pulses for a 1 nm Ag and 5 nm thick Co configuration. The early stage dewetting morphology, evidenced by the morphology after 10 and 100 laser pulses (Figure 1a,b), shows a network of holes or polygons. The final stable morphology, obtained after long irradiations ( $\sim 10\,000$ , Figure 1c) consists of an array of nanoparticles. The spatial characteristic of each morphology was obtained by evaluating the fast Fourier transform (FFT) of the contrast in the SEM image. The FFT information of the contrast correlation is shown in the inset of each figure. The annular form of each FFT indicates the presence of short-range spatial order (SRO) in each stage of dewetting. As shown by previous authors,<sup>9,14</sup> this spatial correlation is evidence that the patterns form via self-organization rather than by homogeneous nucleation and growth, which will typically lead to particles with no correlation in their interparticle spacings. Similar to AGCO, the progression of dewetting morphology was also studied for the Co/Ag/SiO<sub>2</sub> bilayer, as shown in Figure 1d–f. Here the SEM images (d–f) correspond to irradiation by 10, 100, and 10 000 pulses, respectively, for the 5 nm Ag and 1.5 nm Co configuration. In contrast to the AGCO, the morphology evolution here proceeds by the formation of bicontinuous structures. However, spatial SRO is still evident, as seen by the annular form of the FFT (inset of Figure 1d–f).

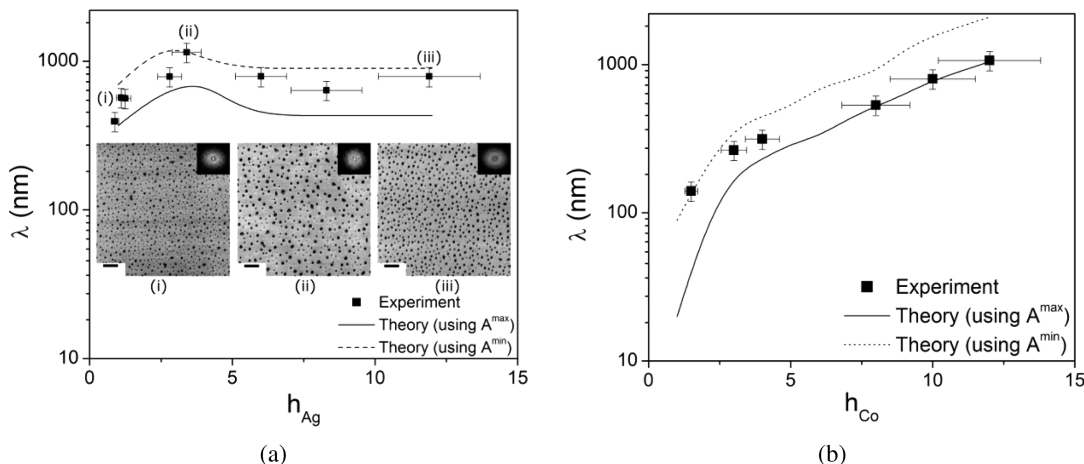


**Figure 2.** (a) Experimentally determined interparticle spacings (closed squares) for Ag/Co/SiO<sub>2</sub>. The SEM micrographs in the inset show the difference in particle spacing for various top Ag layer thickness. The scale bar in each SEM is 2000 nm. The theoretical predictions are shown by the dashed and dotted lines and correspond to the minimum ( $|5 \times 10^{-19}|$  J) and maximum ( $|5 \times 10^{-18}|$  J) magnitudes of the Hamaker coefficient. (b) Experimentally determined interparticle spacings (closed squares) for Co/Ag/SiO<sub>2</sub>. The theoretical predictions are shown by the dashed and dotted lines and again correspond to the minimum and maximum  $A$ 's. In both cases, the bottom layer thickness was kept constant at 5 nm and the top layer thickness was varied.

A detailed investigation of the morphology evolution as a function of film thickness and bilayer configuration suggested that the morphological pathway depends primarily on the ratio of Co to Ag thickness in the bilayer. When Co is thicker than Ag, the evolution is by the formation of holes and polygon networks. This is similar to the case of morphological evolution by spinodal dewetting in single layer Co on SiO<sub>2</sub>.<sup>14,15</sup> Likewise, when the Ag film is thicker than the Co film, the morphology pathway is *via* the formation of bicontinuous structures (Figure 1d,e). This behavior is consistent with spinodal dewetting of single layer Ag, which shows bicontinuous structures.<sup>22</sup> The reason for bicontinuous *versus* hole-type patterns has been attributed to a film-thickness-dependent free energy shape local minima. When the film thickness lies to the left of the free energy minima, bicontinuous structures are found to result, while for films with thickness to the right of the minima, hole-type patterns result.<sup>13,22,23</sup> It is highly likely that similar reasoning underlies the behavior for the bilayer system.

In the inset of Figure 2a, the final nanoparticle state for AGCO with a fixed bottom Co layer thickness of 5 nm is shown for three different Ag thicknesses. While an increase in interparticle spacing is evident in going from 1 to 3.5 nm Ag, a decrease is evident in going from 3.5 to 12 nm. The final interparticle spacing with increasing top layer Ag thickness AGCO is shown in Figure 2a by the closed squares. It is evident that the trend is nonmonotonic, with a change in trend around 4 nm Ag, after which the length scale decreases and eventually saturates with increasing top layer thickness. In contrast, for COAG, the length scale increases monotonically over the range investigated (Figure 2b, closed squares). In order to explain this dramatic difference in length scale behavior with change in arrangement of

the metals in the bilayer, we have resorted to ER theory.<sup>21,24</sup>

**Theory.** For these thin films, the ER theory was applied within the lubrication approximation and with neglection of inertial effects.<sup>25</sup> As a consequence, the primary energy loss mechanism during fluid flow is due to viscous dissipation. The bilayer arrangement and various quantities shown in Figure 3a were used to evaluate  $\Delta F$  and  $E_V$ . Here, the initially flat film thicknesses for bottom layer and the total layer is indicated as  $h_{10}$  and  $h_{20}$ , respectively. The competing forces in this SO were considered to be the surface or interfacial tensions and the long-range intermolecular dispersion forces between the various interfaces.<sup>17</sup> The surface tensions corresponding to the liquid<sub>1</sub>–liquid<sub>2</sub> and liquid<sub>2</sub>–gas interfaces are  $\gamma_{12}$  and  $\gamma_2$ , respectively. The three relevant dispersive forces, expressed in sign and magnitude by the Hamaker coefficient, are  $A_{g2}$ ,  $A_{gsr}$ , and  $A_{2s}$ , which correspond to interactions between the top-middle, top-substrate, and middle-substrate interfaces, respectively, as depicted in Figure 3a. The signs of these interactions for the two bilayer systems studied are tabulated in Figure 3b. The subscripts g, 2, and s denote the gas–liquid 2 (top layer), liquid 2–liquid 1 (bottom layer), and liquid 1–substrate interfaces, respectively. The middle liquid 1/liquid 2 interface and top free liquid surfaces are perturbed by Fourier components of type  $h_1 = h_{10} + \varepsilon_1 e^{i\alpha t - ikx}$  and  $h_2 = h_{20} + \varepsilon_2 e^{i\alpha t - ikx}$ , where the perturbation amplitudes are  $\varepsilon_1$  and  $\varepsilon_2$ , respectively. The collective modes for deformation have been considered,<sup>17,19</sup> wherein the decay rate and wave vector are identical for the two surfaces for the two possible deformation modes corresponding to the situations when the perturbation amplitude ratio  $\alpha = \varepsilon_1/\varepsilon_2$  is  $>0$ , also known as the bending mode, or when  $\alpha < 0$ , also known as the squeezing mode (shown in Figure

3a). While the complete derivation is provided in the Supporting Information, the key steps are noted here. First,  $\Delta F$  due to change from the flat unperturbed state to the perturbed state of the films is obtained as<sup>20</sup>

$$\Delta F = \sigma \varepsilon_1^2 \left[ \gamma_2 \alpha^2 k^2 + \gamma_{12} k^2 + \frac{A_{gs} \alpha^2}{2\pi h_{20}^4} + \frac{A_{2s}}{2\pi h_{10}^4} + \frac{A_{g2}(\alpha - 1)^2}{2\pi(h_{20} - h_{10})^4} \right] e^{2\alpha t - 2ikx} = \sigma \varepsilon_1^2 [dF] e^{2\alpha t - 2ikx}$$

where  $dF = \gamma_2 \alpha^2 k^2 + \gamma_{12} k^2 + \frac{A_{gs} \alpha^2}{2\pi h_{20}^4} + \frac{A_{2s}}{2\pi h_{10}^4} + \frac{A_{g2}(\alpha - 1)^2}{2\pi(h_{20} - h_{10})^4}$  (1)

Next, the total viscous dissipation  $E_V$  for the bilayer fluid flow is evaluated from knowledge of the viscous stresses within each of the two fluid layer as

$$E_V = \eta_1 \int_0^{h_{10}} \left( \frac{du_1}{dz} \right)^2 dz + \eta_2 \int_{h_{10}}^{h_{20}} \left( \frac{du_2}{dz} \right)^2 dz \quad (2)$$

In order to calculate this, we have assumed an isothermal situation. The boundary conditions and resulting expression for velocities are taken from Bando-padhyay *et al.*<sup>17</sup> The top surface is considered stress free, and the bottom liquid-substrate interface is a no-slip interface, while for the middle interface between the two liquids, the stress and velocity are continuous. By making use of volume conservation of the fluid within each layer, the total viscous dissipation for the bilayer can be written as<sup>21</sup>

$$E_V(k, \alpha) = -R \left( \frac{\sigma^2 \varepsilon_1^2}{k^2} \right) e^{2\alpha t - 2ikx} \quad (3)$$

where,  $R$  is a function of  $f(h_{10}, h_{20}, \eta_1, \eta_2, \alpha)$  and is detailed in the Supporting Information.

Finally, the dispersion relation that relates the rate of deformation  $\sigma$  with the wave vector  $k$  is obtained by equating  $\Delta F$  (eq 1) to  $E_V$  (eq 3) with the resulting expression being of form

$$\sigma(k, \alpha) = -\frac{k^2 dF}{R} \quad (4)$$

From the form of eq 4, it can be noted that the deformation rate  $\sigma$  is a function of two variables,  $k$  and  $\alpha$ , for any given value of  $h_{10}$  and  $h_{20}$ . Therefore, in order to obtain the most probable length scale  $\lambda$ , the maximum deformation rate must be obtained from a surface plot of  $\sigma$  versus  $k$  and  $\alpha$ . Mathematically, the maxima of this function is obtained by simultaneously solving for  $\partial\sigma/\partial\alpha = 0$  and  $\partial\sigma/\partial k = 0$  and evaluating the critical point for the maximum. In this work, we have numerically obtained this maxima value in order to generate the theoretical length scales of pattern formation, used in Figure 2.

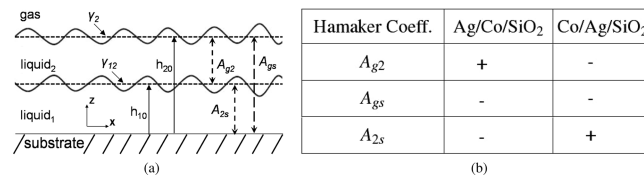
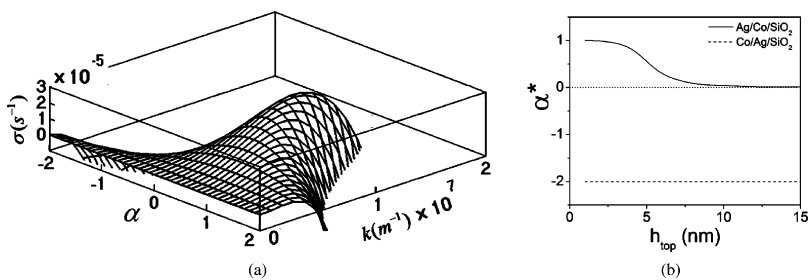


Figure 3. (a) Schematic of the bilayer arrangement. The perturbation depicted by solid surfaces is a squeezing mode ( $\alpha = \varepsilon_2/\varepsilon_1$  is  $<0$ ). (b) Table depicting the signs of the Hamaker coefficients for the various pairs of interfaces in (a). A negative sign corresponds to a destabilizing attractive interaction.

## DISCUSSION AND CONCLUSIONS

In Figure 3b, the signs of  $A$  for the two bilayers are presented. It is important to note here that, while signs are fixed, the magnitude of the Hamaker coefficient values can be obtained by several approaches. Theoretically, the  $A$  values can be calculated using the dielectric function of the different materials involved, as shown in ref 18, while in ref 17, they are evaluated using the various interfacial energies. In addition, indirect experimental values based on dewetting studies yield yet another value of  $A$ .<sup>20</sup> As a result, the magnitude of  $A$  can range between  $A^{\min} = 5 \times 10^{-19}$  and  $A^{\max} = 5 \times 10^{-18}$  J. Here, we have estimated the theoretical behavior for these two extremes of the  $A$  values. The two extreme dispersion curves for each bilayer system are shown as the dashed and dotted lines in Figure 2a,b. The viscosities and surface tensions used in the calculations are  $\eta_{Co} = 4.46 \times 10^{-3}$  Pa·s;  $\eta_{Ag} = 3.88 \times 10^{-3}$  Pa·s;  $\gamma_{Co} = 1.88$  J m<sup>-2</sup>;  $\gamma_{Ag} = 0.925$  J m<sup>-2</sup>; and  $\gamma_{Ag/Co} = \gamma_{Co/Ag} = 0.168$  J m<sup>-2</sup>. In Figure 4a, a typical 3-D dispersion plot is shown for the bilayer case of Ag(5 nm)/Co(5 nm)/SiO<sub>2</sub> using  $A$  values calculated using ref 18. It is evident that, for a specific combination of  $k$  and  $\alpha$ , the deformation rate attains a maximum. From such 3-D dispersion plots, the location of the maxima characterized by the rate  $\sigma^*$ , wave vector  $k^*$ , and the corresponding  $\alpha^*$  value could be evaluated for any combination of bilayer thickness and bilayer arrangement. The conventional representation of this dispersion plot in 2-D will be a slice taken at  $\alpha^*$ . In Figure 4b, the value of  $\alpha^*$  corresponding to the dispersion maxima for the two bilayer systems is plotted. From this, it is evident that the AGCO deforms by the bending mode ( $\alpha > 0$ ), while COAG deforms by the squeezing mode ( $\alpha < 0$ ). We also found that the value of  $\alpha^*$  was virtually independent of the  $A$  value used for the numerical calculations.

From the dispersion plots, the theoretical behavior of the length scale  $\lambda$  for the two bilayer arrangements was generated and is shown in Figure 2a,b as the dotted and dashed lines, corresponding to the minimum and maximum magnitudes of  $A$ . As is evident, for the AGCO case (Figure 2a), an initial increase in length scale with increasing thickness is followed by a dramatic decrease and subsequent saturation in length scales for large Ag thickness. This change in behavior occurs when the top Ag layer thickness is  $\sim 4$  nm. This theoretical behavior, including the location of the change in



**Figure 4.** (a) Surface plots of the dispersion behavior showing variation in the decay rate  $\sigma$  as a function of wave vector  $k$  and perturbation amplitude ratio  $\alpha$  for  $\text{Ag}(5 \text{ nm})/\text{Co}(5 \text{ nm})/\text{SiO}_2$ . (b) Sign and magnitude of  $\alpha^*$ , which characterizes the type of collective deformation, obtained at the dispersion maximum for the two bilayer systems. For  $\text{Ag}/\text{Co}/\text{SiO}_2$ , the collective mode is a bending mode over the entire thickness range, while it is a squeezing mode for  $\text{Co}/\text{Ag}/\text{SiO}_2$ .

trend, is in good agreement with the experimental results (Figure 2a, solid squares). On the other hand, the length scale for the case of COAG increases steadily with increasing Co thickness (Figure 2b). Once again, theory is in good agreement with experiments (Figure 2b, solid squares).

The difference in SO behavior for the two bilayers can be explained on the basis of the difference in intermolecular forces. As shown in Figure 3b, the signs (negative sign is a destabilizing attractive interaction, while positive is repulsive) of the intermolecular dispersion forces are different for the two arrangements. In the case of COAG, the gas-middle ( $A_{g2}$ ) and gas-substrate ( $A_{gs}$ ) interfaces are always destabilizing because of the negative  $A$ 's, while the middle-substrate layer ( $A_{2s} > 0$ ) is always stabilizing. As a result, the spontaneous patterning is dictated primarily by the top layer and so the length scale increases monotonically with top Co layer thickness. For the case of AGCO, the gas-substrate ( $A_{gs}$ ) and middle-substrate interfaces ( $A_{2s}$ ) are destabilizing, while the gas-middle ( $A_{g2}$ ) is stabilizing ( $> 0$ ). In this case, when the top layer (Ag) is thin compared to the bottom layer (Co), the  $A_{gs} < 0$  destabilizes the bilayer. The length scale increases with increasing

top layer (Ag) thickness up to the point when the contribution of  $A_{gs}$  is sufficiently weak, so that the instability is then determined primarily by the bottom ( $A_{2s}$ ) Co layer. In the case of Ag/Co, this transition is predicted to occur when the top layer thickness is  $\sim 4 \text{ nm}$  (Figure 2a). At the point of the transition, the patterning length scale will then readjust or saturate to a value determined by the fixed thickness of the bottom layer. This behavior is predicted by the theory, as seen by the saturation of the dashed (or solid) line in Figure 2a after  $\sim 6 \text{ nm}$  thick Ag films and is also evident in the experimental behavior. We have shown recently that nanoscale effects from nanosecond laser heating of single layer metallic film can lead to intrinsic thermal gradients and consequently modify patterning length scales.<sup>11,20</sup> While accurate thermal models will likely improve the quantitative agreements, the simple isothermal ER model presented here has visibly captured the essential behavior of the bilayer patterning process.

We have also compared the behavior of experiment with theory for the COAG system in which the Co and Ag films have approximately similar film thickness, but the overall film thickness is varied in the range of 4 to 20 nm. The experimental trend is shown in Figure 5 (symbols), while the theoretical trends are shown as the dashed and solid lines in this figure. As mentioned above, the behavior of the COAG system is dominated by the top Co layer. Therefore, we have evaluated the theoretical trends as follows. The solid line corresponds to the theory trend calculated using a Hamaker coefficient value of  $A^{\max} = -5 \times 10^{-18} \text{ J}$  for the top Co (or  $A_{g2}$ ) layer, while the dashed line corresponds to  $A^{\min} = -5 \times 10^{-19} \text{ J}$  for the  $A_{g2}$  layer. Here, the  $A_{gs}$  and  $A_{2s}$  values were kept fixed at  $-2.03 \times 10^{-19}$  and  $6.07 \times 10^{-19}$  and were calculated based on the approach in ref 17. A good agreement can be seen between the experimental trend and the theory trend with  $A^{\max}$ .

In summary, we have explored spontaneous patterning of bilayer metallic liquids of nanoscopic thickness under nanosecond pulsed laser heating. Co and Ag metals were chosen for their immiscibility. The patterning behavior was different for the two possible bilayer arrangements. We have understood this by developing the bilayer energy rate model of self-organization, in

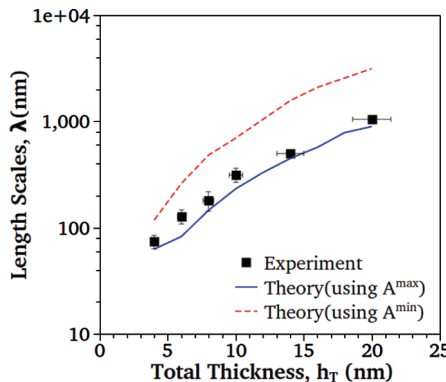


**Figure 5.** Comparison of experiment (symbols) with theoretical trends (dashed and solid lines) for the  $\text{Co}/\text{Ag}/\text{SiO}_2$  system (COAG) in which the total thickness is varied between 4 to 20 nm and the individual films are of comparable thickness. The solid line corresponds to the theory trend calculated using a Hamaker coefficient value of  $A^{\max} = -5 \times 10^{-18} \text{ J}$  for the  $A_{g2}$  layer, while the dashed line corresponds to  $A^{\min} = -5 \times 10^{-19} \text{ J}$  for the  $A_{g2}$  layer. Here, the  $A_{gs}$  and  $A_{2s}$  values are  $-2.03 \times 10^{-19}$  and  $6.07 \times 10^{-19}$  and were calculated based on the approach in ref 17.

which the rate of Gibbs energy change is balanced by viscous dissipation. The theory predictions were in very good agreement with experiments, including capturing the different behaviors of the two bilayers. Differences in the sign of the intermolecular forces between the two arrangements leads to a change in the mode of deformation for the two cases and different patterning behavior. As a result, it is possible to vary the length scales for identical values of film

thickness by simply interchanging the two layers. We also found that the morphological pathway for pattern formation was dictated by the thicker film in the bilayer. Consequently, either holes or bicontinuous structures were visible during the early stages of pattern formation. These type of bilayer arrangements could be useful toward independently manipulating the composition as well as the length scales of nanoscale mixtures and alloys.

## EXPERIMENTAL METHODS

Thin films of Co and Ag were deposited under ultrahigh vacuum ( $\sim 1 \times 10^{-8}$  Torr) using electron beam evaporation (e-beam) and pulsed laser deposition (PLD) techniques on commercially available and optically smooth 400 nm  $\text{SiO}_2$  on Si(100) substrates. For AGCO experiments, a bottom Co film of 5 nm was deposited on the substrates by e-beam, followed by the deposition of a top Ag layer by PLD with film thicknesses varying from 1 to 12 nm. Similarly, for COAG, a 5 nm Ag bottom layer was deposited by e-beam, followed by deposition of the top layer Co film via PLD with the same thickness range (1–12 nm). The verification of thicknesses and smoothness have been described in detail previously.<sup>15</sup> The samples were irradiated in vacuum with a uniform Nd:YAG laser beam at normal incidence with 266 nm wavelength, pulse width of 9 ns, and repetition rate of 50 Hz. The laser energy density was between 80 and 100  $\text{mJ/cm}^2$ , chosen such that the entire bilayer could be melted for all the thickness combinations, as evidenced by a visible morphology change.<sup>14</sup> The morphology evolution was studied as a function of the number of laser pulses  $n$ , which typically ranged between 10 and 10 000 pulses, with the upper limit used to create the final stable array of nanoparticles for all of the bilayers. The patterns were then characterized using a Hitachi S-4300 scanning electron microscope (SEM). We have previously reported a transmission electron microscopy result for a single Ag/Co/ $\text{SiO}_2$  film in which we confirmed that there was no evidence for chemical interaction between the metals or with the substrate.<sup>26</sup>

**Acknowledgment.** The authors acknowledge support by the Sustainable Energy Education and Research Center, Center for Materials Innovation, and the NSF through grants CAREER DMR-0449258, CMMI-0855949, and DMR-0805258.

**Supporting Information Available:** We have provided a detailed derivation of the energy rate model for the bilayer self-organization theory discussed in the Results section. This material is available free of charge via the Internet at <http://pubs.acs.org>.

## REFERENCES AND NOTES

1. Zayats, M.; Pogorelova, S.; Kharitonov, A.; Lioubashevski, O.; Katz, E.; Willner, I. A Nanoparticle-Enhanced Surface Plasmon Resonance Sensing of Biocatalytic Transformations. *Chem.—Eur. J.* **2003**, *9*, 6108–6114.
2. Hirsch, R.; Katz, E.; Willner, I. Magneto-Switchable Bioelectrocatalysis. *J. Am. Chem. Soc.* **2000**, *122*, 12053–12054.
3. Seydack, M. Nanoparticle Labels in Immunosensing Using Optical Detection Methods. *Biosens. Bioelectron.* **2005**, *20*, 2454–2469.
4. Safarov, V. I.; Kosobukin, V. A.; Hermann, C.; Lampel, G.; Peretti, J.; Marliere, C. Magneto-Optical Effects Enhanced by Surface Plasmons in Metallic Multilayer Films. *Phys. Rev. Lett.* **1994**, *73*, 3584–3587.
5. Abe, M.; Suwa, T. Surface Plasma Resonance and Magneto-Optical Enhancement in Composites Containing Multicore–Shell Structured Nanoparticles. *Phys. Rev. B* **2004**, *70*, 235103.
6. Albert, F. J.; Katine, J. A.; Buhrman, R. A.; Ralph, D. C. Spin-Polarized Current Switching of a Co Thin Film Nanomagnet. *Appl. Phys. Lett.* **2000**, *77*, 3809–3811.
7. Rusponi, S.; Boragno, C.; Valbusa, U. Ripple Structure on Ag(110) Surface Induced by Ion Sputtering. *Phys. Rev. Lett.* **1997**, *78*, 2795–2798.
8. Facsko, S.; Kurz, H. Energy Dependence of Quantum Dot Formation by Ion Sputtering. *Phys. Rev. B* **2001**, *63*, 165329-1–165329-5.
9. Herminghaus, S.; Jacobs, K.; Mecke, K.; Bischof, J.; Fery, A.; Ibn-Elhaj, M.; Schlagowski, S. Spinodal Dewetting in Liquid Crystal and Liquid Metal Films. *Science* **1998**, *282*, 916–919.
10. Favazza, C.; Trice, J.; Kalyanaraman, R.; Sureshkumar, R. Self-Organized Metal Nanostructures through Laser-Interference Driven Thermocapillary Convection. *Appl. Phys. Lett.* **2007**, *91*, 043105.
11. Trice, J.; Favazza, C.; Thomas, D.; Garcia, H.; Kalyanaraman, R.; Sureshkumar, R. Novel Self-Organization Mechanism in Ultrathin Liquid Films: Theory and Experiment. *Phys. Rev. Lett.* **2008**, *101*, 017802.
12. Vrij, A. Possible Mechanism for the Spontaneous Rupture of Thin, Free Liquid Films. *Discuss. Faraday Soc.* **1966**, *42*, 23–27.
13. Sharma, A.; Khanna, R. Pattern Formation in Unstable Thin Liquid Films. *Phys. Rev. Lett.* **1998**, *81*, 3463–3466.
14. Favazza, C.; Kalyanaraman, R.; Sureshkumar, R. Robust Nanopatterning by Laser-Induced Dewetting of Metal Nanofilms. *Nanotechnology* **2006**, *17*, 4229.
15. Trice, J.; Thomas, D.; Favazza, C.; Sureshkumar, R.; Kalyanaraman, R. Pulsed-Laser-Induced Dewetting in Nanoscopic Metal Films: Theory and Experiments. *Phys. Rev. B* **2007**, *75*, 235439.
16. Gonzalez-Diaz, J. B.; Garcia-Martin, A.; Garcia-Martin, J. M.; Cebollada, A.; Armelles, G.; Sepulveda, B.; Alaverdyan, Y.; Kall, M. Plasmonic Au/Co/Au Nanosandwiches with Enhanced Magneto-optical Activity. *Small* **2008**, *4*, 202–205.
17. Bandyopadhyay, D.; Gulabani, R.; Sharma, A. Instability and Dynamics of Thin Liquid Bilayers. *Ind. Eng. Chem. Res.* **2005**, *44*, 1259.
18. Pototsky, A.; Bestehorn, M.; Merkt, D.; Theile, U. Alternative Pathways of Dewetting for a Thin Liquid Two-Layer Film. *Phys. Rev. E* **2004**, *70*, 025201.
19. Brochard Wyart, P.; Martin, F.; Redon, C. Liquid/Liquid Dewetting. *Langmuir* **1993**, *9*, 3682–3690.
20. Krishna, H.; Shirato, N.; Favazza, C.; Kalyanaraman, R. Energy Driven Self-Organization in Nanoscale Metallic Liquid Films. *Phys. Chem. Chem. Phys.* **2009**, *8*, 8136–8143.
21. Shirato, N.; Krishna, H.; Kalyanaraman, R. Thermodynamic Approach to the Dewetting Instability in Ultrathin Film. *J. Appl. Phys.* **2010**, *108*, 024313.
22. Krishna, H.; Sachan, R.; Strader, J.; Favazza, C.; Khenner, M.; Kalyanaraman, R. Thickness-Dependent Spontaneous Dewetting Morphology of Ultrathin Ag Films. *Nanotechnology* **2010**, *21*, 155601.
23. Seemann, R.; Herminghaus, S.; Jacobs, K. Gaining Control of Pattern Formation of Dewetting Liquid Films. *J. Phys.: Condens. Matter* **2001**, *13*, 4925–4938.

24. de Gennes, P. G. Wetting: Statics and Dynamics. *Rev. Mod. Phys.* **1985**, *57*, 827–863.
25. Kondic, L. Instabilities in Gravity Driven Flow of Thin Fluid Films. *SIAM Rev.* **2003**, *45*, 95–115.
26. Krishna, H.; Favazza, C.; Gangopadhyay, A.; Kalyanaraman, R. Functional Nanostructures through Nanosecond Laser Dewetting of Thin Metal Films. *JOM* **2008**, *60*, 37–42.